CHEMISTRY OF MATERIALS

pubs.acs.org/cm

Article

High-Pressure Synthesis of Polar and Antiferromagnetic Mn_2MnMoO_6

Shuang Zhao, Jin-Jin Yang, Yi-Feng Han,* Mei-Xia Wu, Mark Croft, Peter W. Stephens, David Walker, Martha Greenblatt,* and Man-Rong Li*

Cite This: *Chem. Mater.* 2022, 34, 1930−1936

Read Online

ACCESS | Metrics & More | Article Recommendations | Supporting Information

ABSTRACT: Polar and magnetic Mn_2MnMoO_6 with a Ni_3TeO_6-type structure ($R3$) was synthesized at 1673 K under 8 GPa. Mn_2MnMoO_6 shows a large spontaneous polarization of 65.76 $\mu C \cdot cm^{-2}$, two magnetic transitions at 19 and 47 K, and a strong magnetic frustration factor (f) of 18.4. The polarization reversal barrier is estimated to be 232 meV. X-ray absorption spectroscopy established $Mn_2^{2+}Mn^{2+}Mo^{6+}O_6$ formal oxidation states. Theoretical calculations indicate an antiferromagnetic ground state of up−down−up−down−up−down spin alignment for Mn ions and a semiconductor characteristic with a band gap around 1.06 eV. Magnetism-dependent dielectric responses show no magnetodielectric and electric coupling, which is attributed to the high polarization reversal barrier and grain boundary effects.

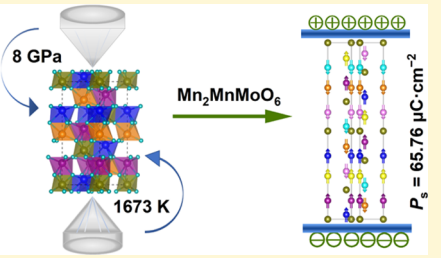

INTRODUCTION

Polar corundum derivatives can integrate spontaneous polarization (P_S) and magnetism in the same lattice, providing an ideal platform to design technologically important multiferroics.[1−6] The geometric feature (small A-site) of the corundum-based family enables efficient occupation of all cationic sites by magnetic ions, as realized in high pressure and temperature (HPT) synthesized Mn_2FeMoO_6.[7,8] $Mn_2^{2+}Fe^{3+}MoO_6^{5+}$ prepared at 8 GPa and 1623 K adopts the ordered double corundum structure ($R3$) with about 7% Fe/Mo antisite disordering. The interactions between high-spin (HS) d^5-Mn^{2+}, Fe^{3+}, and d^1-Mo^{5+} render a ferrimagnetic ordering up to $T_C \sim 340$ K, making it the only double perovskite-related above room temperature (RT) ferrimagnetic−multiferroic material to the best of our knowledge.[7] The thermal treatment of Mn_2FeMoO_6 at ambient pressure (AP) initiated an unprecedented cationic redistribution between 423 and 573 K in that 88% of the Mn^{2+} and Fe^{3+} in the face-shared octahedral pair switched positions, accompanied by a phase transition from Ni_3TeO_6 (NTO)-type to an ordered ilmenite (OIL, $R3$) structure. Accordingly, resistivity of the OIL polymorph was found to be around three orders of magnitude higher than that of the NTO counterpart, accompanied with the magnetic ordering temperature dropping from ∼340 to 229 K.[8] Replacement of Mo by W in Mn_2FeMoO_6 via HPT (8 GPa and 1673 K) preparation led to the discovery of isostructural NTO-type $Mn_2^{2+}Fe^{2+}W^{6+}O_6$, which is antiferromagnetic (AFM) below 70 K and demonstrates magnetic-field-dependent and complicated metamagnetism.[9] Theoretical calculations suggested that the proposed optimal switching path displays a metallic intermediate state in Mn_2FeWO_6 and thus hinders possible ferroelectricity.[9] In contrast, magnetostriction polarization and magnetoelectric coupling were observed for the first time in the AFM (T_N = 58 K) Mn_2MnWO_6 among the NTO-type double corundum family.[10] Attempts to replace Mo and W by Re in the above compounds yielded centrosymmetric monoclinic ($P2_1/n$) perovskite Mn_2FeReO_6 and Mn_2MnReO_6 rather than the expected NTO polymorphs.[11−14] Apparently, the crystal structures and physical properties of transition-metal-enriched double polar corundum subtly depend on the atomic-scale local structure and electron configuration of cations. In this work, we report the preparation of a new NTO-type Mn_2MnMoO_6 by the HPT approach and experimentally and theoretically study its structure and physical properties.

EXPERIMENTS AND METHODS

Mn_2MnMoO_6 was synthesized via a stoichiometric mixture of MnO (Alfa Aesar, 99.99%) and MoO_3 (Alfa Aesar, 99.95%) by the HPT method. The raw materials were well mixed and sealed in a Pt capsule and then loaded into a MgO crucible. The crucible was placed in a Walker-type multianvil instrument to prepare the polycrystalline sample at 1573 K under 8 GPa for 30 min, as applied in our previous work.[8,15]

RT synchrotron powder X-ray diffraction (RT-SPXD) data for Mn_2MnMoO_6 were recorded on beamline X-16C (λ = 0.69991 Å) at the Brookhaven National Synchrotron Light Source (NSLS-I). TOPAS-Academic *V6* software package[16] was used to analyze the

Received: December 20, 2021
Revised: January 19, 2022
Published: January 31, 2022

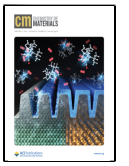

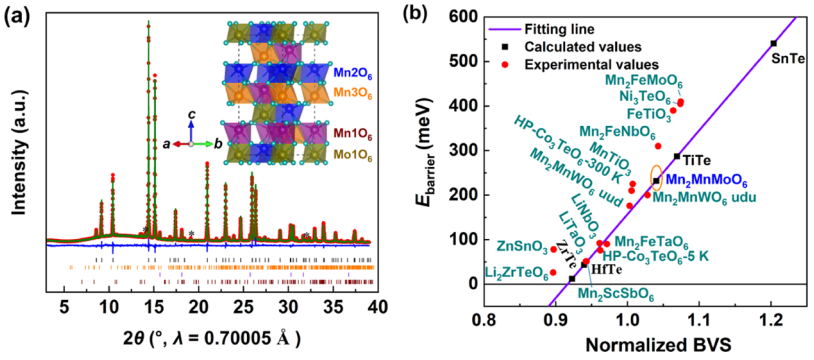

Figure 1. (a) Rietveld refinements of RT-SPXD patterns for Mn_2MnMoO_6. The observed data are shown as red points; calculated fitting is displayed as an olive line; blue line is the difference; black vertical ticks are Bragg reflections corresponding to the reflection of Mn_2MnMoO_6; orange ticks correspond to the reflection of α-$MnMoO_4$ ($C2/m$, 0.35%);[32,33] violet ticks represent Bragg reflections of MnO ($Fm\bar{3}m$, 3.73%),[31] and wine ticks are consistent with β-$MnMoO_4$ ($P2/c$, 2.02%).[34] "*" Represents an unknown impurity. (b) Comparison of $E_{barrier}$ between Mn_2MnMoO_6 and other polar-corundum compounds.[5,10,36−38] Reprinted with permission from ref 38. Copyright 2021 American Chemical Society.

RT-SPXD data. X-ray absorption near-edge spectroscopy (XANES) measurements of Mn_2MnMoO_6 and standards were performed on beamline X-19A at the Brookhaven National Synchrotron Light Source (NSLS-I) with a Si-111 double crystal monochromator. The Mn-K XANES data were collected in both the transmission and fluorescence mode with simultaneous standards. The Mo-L_3 XANES data were collected in fluorescence mode in a He atmosphere with sequential standards. All data were fitted and normalized to pre- and post-edge background and unity absorption edge step across the edge, respectively.[7,17−22]

Density functional theory (DFT) calculations were performed by VASP.[23−26] Based on the projector augmented-wave (PAW) method,[27,28] the plane wave cut-off energy was set as 600 eV. The exchange correlation energy was treated by the generalized gradient approximation (GGA-PBE).[29] A mesh of 5 × 5 × 5 k-points was used for geometry optimization and static electronic calculations. The convergence threshold was set to be 1.0×10^{-6} eV in energy and 1.0×10^{-2} eV/A in force, respectively. Electron−electron Coulombic repulsion interactions (U) for Mn were considered in the rotationally invariant form (GGA + U)[30] with U_{Mn} = 4.2 eV.

Magnetic properties were measured in a Physical Properties Measurement System (PPMS-9T, Quantum Design). Temperature-dependent data of zero-field-cooled (ZFC) and field-cooled (FC) susceptibility were measured from 10 to 300 K with an external magnetic field of 0.1 T. Isothermal magnetization curves were collected at different temperatures with the field from −3.6 to 3.6 T. The temperature-dependent magnetodielectric response was measured with an α-A analyzer in the same PPMS equipment from 10 to 300 K with different fields of 0, 1, 3, and 5 T. Frequency-dependent permittivity was also examined with the same system.

RESULTS AND DISCUSSION

RT-SPXD data refinements indicate that Mn_2MnMoO_6 adopts a polar rhombohedral structure with space group $R3$ (No. 146) as shown in Figure 1a, giving a 93.9 wt % target phase, 6.10 wt % impurity (MnO, $Fm\bar{3}m$,[31] 3.73%; α-$MnMoO_4$, $C2/m$,[32,33] 0.35%; β-$MnMoO_4$, $P2/c$,[34] 2.02%), and tiny unidentified peaks. All cations located at A (Mn1 and Mn2 at 3a (0, 0, z)) and B (Mn3 at 3a (0, 0, z) and Mo at 3a (0, 0, 0)) sites are in ordered arrangement in the crystal structure of Mn_2MnMoO_6. The oxygen atoms are located at two positions at 9b (x, y, z) derived from the higher degree of cation order. Table S1 lists the specific atomic positions and structural parameters for Mn_2MnMoO_6, which is isostructural with other NTO-type analogues, such as Mn_2FeMoO_6,[7] Mn_2FeWO_6,[9] and Mn_2MnWO_6.[10] The edge-sharing connection of $Mn1O_6$/$Mn3O_6$ and $Mn2O_6$/MoO_6 forms honeycomb layers in the ab plane. $Mn1O_6$−MoO_6 and $Mn2O_6$−$Mn3O_6$ pairs are connected through face sharing along the c-axis. Such crowded connection leads to large structural distortions and thus significant differences at metal−oxygen bond distances and angles. As shown in Table S2, the bond distance of Mn−O ranges from 2.050(13) to 2.390(11) Å and that of Mo−O from 1.859(9) to 1.988(18) Å, rendering strong anisotropy and large Ps calculated to be 65.76 $\mu C \cdot cm^{-2}$ by the point charge model.[35] Previous research demonstrates that, for polar-corundum-type derivatives, the polarization reversal barrier ($E_{barrier}$) of the domain wall shows a strong correlation to the local bonding environment of A-site cations, as can be evaluated by normalized bond-valence sums (BVS).[5,9,36−38] On this basis, the $E_{barrier}$ of Mn_2MnMoO_6 is estimated to be about 232 meV (Figure 1b), which is between the values of Mn_2FeMoO_6[5,7] and Mn_2MnWO_6.[10] The average ⟨Mn1−O⟩ bond length (2.170 (15) Å) in Mn_2MnMoO_6 is comparable with those in Mn_2MnWO_6 (2.00 Å)[10] and Mn_2FeMoO_6 (2.195 Å).[7] In contrast, the $Mn2O_6$ octahedron is highly distorted and results in an extra-long average ⟨Mn2−O⟩ (2.220 Å) compared to that in Mn_2MnWO_6 (2.06 Å)[10] and Mn_2FeMoO_6 (2.091 Å). The octahedral distortion parameter Δ (58.64×10^{-4}, $\Delta = (1/n) \times \sum[(d_i - d_{av})/d_{av}]^2$, where d_i is the metal−oxygen bond length and d_{av} is the average bond length)[39] in Mn_2MnMoO_6 implies that $Mn2O_6$ possesses the strongest distortion with off-centered Mn2. The ⟨Mn3−O⟩ (2.217(16) Å) and ⟨Mo−O⟩ (1.933(14) Å) around B/B' sites in Mn_2MnMoO_6 are highly comparable to ⟨Mn3−O⟩ (2.196(2) Å) in Mn_2MnWO_6[10] and ⟨Mo−O⟩ (1.975(4) Å) in MoO_6 octahedra of MoO_3.[40] No Mn−Mo antisite disordering was detected in Mn_2MnMoO_6 within the estimated standard deviation during the refinements, which, together with the shorter Mo−O bond (close to other B-site ordered perovskites) than that in Mn_2FeMoO_6 (around 7% Fe/Mo antisite disorder),[7] implies that the oxidation state of Mo in Mn_2MnMoO_6 is higher than pentavalence. Diversity of bond distances and octahedral distortions among the above three compounds are consistent with completely different physical properties. Crystal structure analyses and BVS[41,42] calculations (Mn1, Mn2, Mn3, and Mo for 2.15, 1.98, 2.08, and 5.83, respectively) suggest a nominal oxidation state of $Mn_2^{2+}Mn^{2+}Mo^{6+}O_6$, which was further confirmed by XANES discussed below.

https://doi.org/10.1021/acs.chemmater.1c04357
Chem. Mater. 2022, 34, 1930−1936

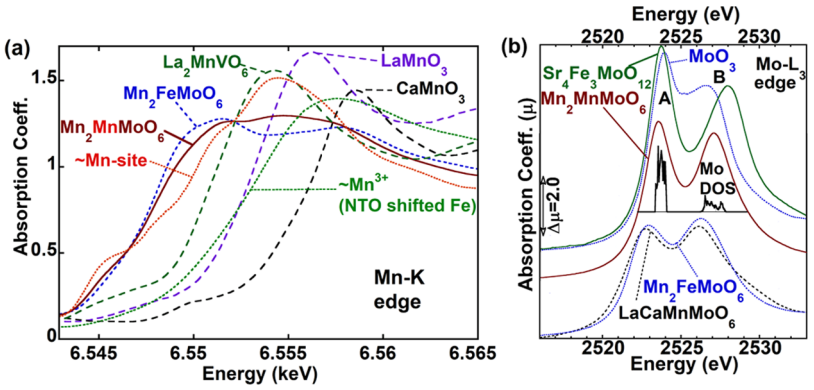

Figure 2. (a) Mn-K edge spectrum for Mn_2MnMoO_6 compared to a series of standard compound spectra: perovskite-based $LaMn^{3+}O_3$, $CaMn^{4+}O_3$, $La_2Mn^{2+}VO_6$, and NTO-type $Mn_2^{2+}Fe^{3+}MoO_6$.[7] The ″~Mn^{3+} (NTO shifted Fe)″ spectrum is the Fe-K edge of the $Mn_2^{2+}Fe^{3+}O_6$ compound shifted down by the energy difference between Fe- and Mn-K edges. The B-site, ″~Mn site″ (dotted red curve), was obtained by subtracting the weighted Mn_2FeMoO_6 from the Mn_2MnMoO_6 followed by renormalization to the conventional unity edge step height. (b) Mo-L_3 edge of Mn_2MnMoO_6 compared with d^0-Mo^{6+} of $Sr_4Fe_3MoO_{12}$ and MoO_3, d^1-Mo^{5+} of Mn_2FeMoO_6 and $LaCaMnMoO_6$. Note that the above E_F Mo d partial DOS, from the DFT calculation below has been included on the same energy scale and that the LF splitting in the XANES agrees well with the calculation.

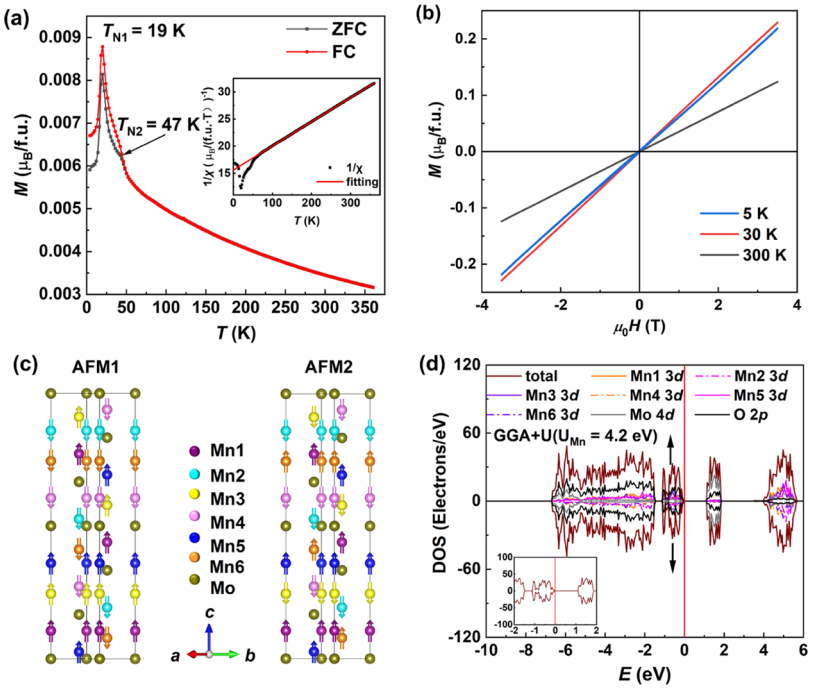

Figure 3. Magnetic behavior and possible magnetic structure of Mn_2MnMoO_6 (a) M vs T curves in ZFC and FC under 0.1 T; inset graph represents the $\chi^{-1}-T$ curves with the Curie−Weiss fitting. (b) Isothermal magnetization curves at different temperatures. (c) AFM1 with ududud order and AFM2 with uddduu order for Mn1, Mn2, Mn3, Mn4, Mn5, and Mn6. (d) Total and partial DOS for Mn_2MnMoO_6 with the AFM1 (ududud) magnetic structure; inset graph illustrates the local amplification for DOS.

The K near edges of 3d transition compounds are dominated by 1s to 4p transition peak features that typically manifest a chemical shift to higher energy with increasing 3d element valence. Figure 2a illustrates the Mn-K near-edge spectra of Mn_2MnMoO_6 and standard compounds with varying Mn valence.[7,19−21] Identifying the spectral components in Mn_2MnMoO_6 is facilitated by comparison with the NTO-type $Mn_2^{2+}Fe^{3+}MoO_6$ standard spectrum.[7] The Mn-K edge of Mn_2MnMoO_6 displays an onset and features similar (albeit reduced) to those of Mn_2FeMoO_6. A similar comparison between Mn_2MnWO_6 and Mn_2FeWO_6 was used to identify the valence of the A-site Mn.[10] Hence, it is clear that the A-site Mn in Mn_2MnMoO_6 is Mn^{2+}. The contribution of the B-site Mn is estimated with red dots in Figure 2a, which was calculated using $\mu(\sim Mn\ site) = 3\ [\mu(Mn_2MnMoO_6) - 2/3\ \mu(Mn_2FeMoO_6)]$. The result of the estimated ~Mn site spectral contribution is consistent with the Mn^{2+} character. To further perfect this process, a short dashed green line in the figure is defined from the downward shift energy of the Fe-K edge in $Mn_2^{2+}Fe^{3+}MoO_6$, which equals the energy difference between the elemental Fe- and Mn-K edges. This line can be used as an estimation of what Mn^{3+} might look like at the B-site. It is clear that the result strongly eliminates Mn^{3+} at this site and underscores the Mn^{2+} character. Therefore, all of the Mn ions in Mn_2MnMoO_6 are in the Mn^{2+}oxidation state.

https://doi.org/10.1021/acs.chemmater.1c04357
Chem. Mater. 2022, 34, 1930−1936

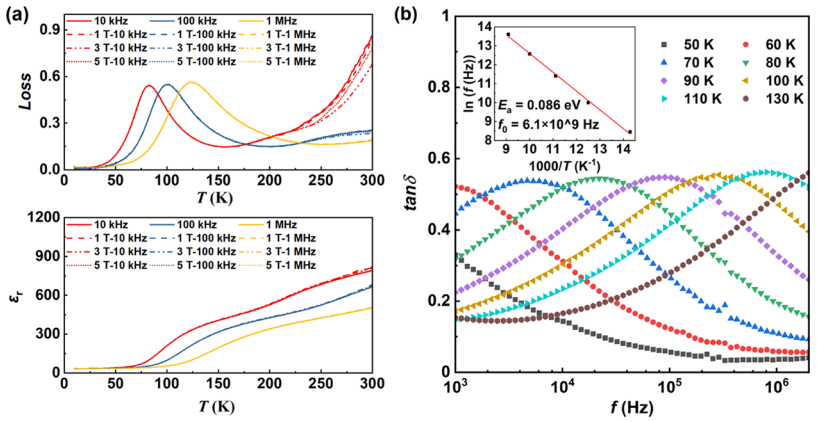

Figure 4. Dielectric measurement results of Mn_2MnMoO_6. (a) ε_r and tan δ vs T under different frequencies and field. (b) Curves of tan δ-dependent frequencies at different temperatures; the inset shows the plot of Arrhenius fitting.

Dipole transitions into final d-states form intense "white line" (WL) peak features, which dominate the L_3 edges of transition compounds. Octahedral O-ligand coordination imposes a ligand field (LF), splitting of the *d*-states, into lower energy, 6X degenerate, t_{2g} and higher energy, 4X degenerate, e_g multiplets. This LF splitting is abundantly clear in Mo-L_3 edge spectra as the splitting of the WL feature into A (t_{2g}-related) and B (e_g-related) features, as illustrated by the Mo-L_3 edges for the ~d^0-Mo^{6+} compounds in Figure 2b (top).[7,17−19,22] In general, increases in the 5d electron count (decreases in the 5d hole count) lead to a reduction in the relative A-feature intensity, although matrix element and bonding/band structure effects can lead to variations in the A−B feature splittings and intensities. Comparing Figure 2b, the general trend of decreasing relative A intensity with decreasing valence (d hole count) can be seen. Another indicator of the Mo d-configuration/valence state is the chemical shift of the WL feature. Comparing Figure 2b top and bottom parts, one should note the systematic chemical shift downward in the WL feature centrum energy between ~d^0-Mo^{6+} and ~d^1-Mo^{5+} standard spectra. The A-feature intensity and chemical shift of the WL feature of the Mn_2MnMoO_6 spectrum in Figure 2b center can clearly be seen to show a ~d^0-Mo^{6+} configuration. This assignment is highly consistent with the Mn^{2+} character at the other cation sites in the compound noted above, in good agreement with the structural analyses and BVS results.

Figure 3a demonstrates the temperature-dependent ZFC and FC magnetization from 4 to 360 K under 0.1 T. Two AFM transition anomalies appear: a sharp peak at 19 K and a clear shoulder at 47 K. The impurity phases are known to show no magnetic transition at these temperatures.[43,44] Therefore, the two transitions are inherent to Mn_2MnMoO_6 induced by the complicated interaction between multiple Mn^{2+} sites. Figure 3a (inset) shows the inverse magnetic susceptibility (χ) and a fit to a Curie−Weiss (CW) model ($\frac{1}{\chi} = \frac{T-\theta}{C}$, with C being the Curie constant, θ being the Curie−Weiss temperature).[45] Fitting the high-temperature range of the $\chi^{-1} - T$ data for the ZFC Mn_2MnMoO_6 case to the CW model fitted for yields of θ = −350 K and C = 12.53 emu·K/(mol·Oe). Thus, Mn_2MnMoO_6 shows an AFM-dominated behavior with an effective magnetic moment (μ_{eff}) of 10.01 μ_B. Here, the much larger magnitude of θ (compared to T_N) supports the presence of substantial magnetic frustration (f = 18.4, $f = |\theta/T_N|$, where θ is the Curie−Weiss temperature and T_N is the Néel temperature).[46] The μ_{eff} is in good agreement with the theoretical value of 10.25 μ_B calculated based on the spin-only response of HS Mn^{2+}. Compared with a similar compound like Mn_3TeO_6 ($R\bar{3}$), where the magnetism is also controlled by three HS Mn^{2+}, Mn_2MnMoO_6 indicates more complex magnetism rooted in the more ordered Mn ions. Antisite disorder and spin−orbit coupling are the key factors for metamagnetism and property diversity.[47−50] Given the d^0-Mo^{6+} ions, the magnetic contribution comes from HS Mn^{2+} only in Mn_2MnMoO_6. Here, the atomic arrangement at the B-site is different from that in Mn_2FeMoO_6, which has a slight antisite disorder. The absence of magnetic contribution from Mo and antisite disorder in Mn_2MnMoO_6 are responsible for the different magnetic features in Mn_2MnMoO_6 compared to Mn_2FeMoO_6. Unlike 5d elements, weaker spin−orbit coupling of 4d elements is one of the factors that result in the absence of complex magnetism like Mn_2MnWO_6 at a low temperature. As shown in Figure 3b, the absence of hysteresis loops in isothermal magnetization curves at a low temperature manifests typical AFM behavior without distinct magnetic competition between AFM and FM interactions.

Considering the representative AFM response in Mn_2MnMoO_6, 11 simple collinear magnetic structures were proposed in the doubled unit cell along the *c*-axis to generate the AFM ordering and simulate the possible magnetic ground state for Mn_2MnMoO_6. For the Mn atom with localized *d* orbitals, the Hubbard U is indispensable for DFT calculations.[9,51] Therefore, a GGA + U methodology was adopted to predict the magnetic moment for each Mn atom and compute the electronic structure. Here, the diversity of spin−orbit coupling in transition elements, orbital hybridization between magnetic and oxygen ions, and magnetic interaction between different magnetic ions were considered to evaluate the influence on the magnetic ground state. The calculated results for all considered AFM and FM ground states are illustrated in Figure S1. As shown in Figure 3c, there are six Mn atoms (labeled as Mn1−Mn6) with different symmetries in the doubled unit cell; the spin directions are set as up−down−up−down−up−down (ududud) and up−down−down−down−up−up (uddduu) as the two representative states, denoted as AFM1 and AFM2, respectively. The calculation results suggest AFM1 as the magnetic ground state, with effective magnetic moments of 4.576, −4.597, 4.535, −4.576, 4.597, and −4.535 μ_B of Mn1, Mn2, Mn3, Mn4,

https://doi.org/10.1021/acs.chemmater.1c04357
Chem. Mater. 2022, 34, 1930−1936

Mn5, and Mn6, respectively, giving the lowest energy (−80.51 eV/f.u.) than other candidates (Figure S2). The difference of the magnetic ground state between Mn_2MnMoO_6, Mn_2MnWO_6,[10] and Mn_2MnSbO_6,[51] which have ududud, noncollinear, and uuuddd AFM ground states, respectively, is one of the main causes for the variation of the magnetic feature. It is well known that the magnetic structures of polar and magnetic corundum derivatives are very subtly sensitive to the electron configuration of each ion—the real situation is complicated case by case.[52−54] Hence, the detailed magnetic structure of Mn_2MnMoO_6 needs further characterizations such as powder neutron diffraction at low temperatures for a clear insight, which is planned in future work.

The total and partial densities of states (DOS) of Mn_2MnMoO_6 are shown in Figure 3d, which illustrates that the band gap for Mn_2MnMoO_6 with the AFM1 ground state is 1.06 eV, implying a semiconducting behavior. The major contributions in the low-energy area of conduction and valence bands from 1 to 2 eV and −7 to −5 eV are generated from the antibonding interaction between Mo-4d and O-2p. In other energy regions, the contribution mainly originates from an interplay between Mn(3d) and O(2p). Hence, the interaction between Mo-4d and O-2p is the main source of semiconductor characteristics. Moreover, the spin of each Mn atom is fully extracted due to the HS-d^5 configuration, which further validates the divalent Mn ions.

The curves of relative permittivity (ε_r) and dielectric loss ($\tan\delta$) vs temperature of Mn_2MnMoO_6 at various frequencies and magnetic fields are shown in Figure 4a. Mn_2MnMoO_6 shows a strong relaxor behavior with large ε_r and low $\tan\delta$. The ε_r values are magnetic-field independent below 250 K, and there are no dielectric anomaly peaks observed around the magnetic transition temperatures (19 and 47 K), which indicate the absence of magnetodielectric and electric couplings. As the temperature increases from 225 to 300 K, the $\tan\delta$ values at low frequency (10 kHz) are significantly larger than the data at higher frequency and exhibit some magnetic-field dependence, which may be due to the extrinsic resistivity and capacitance from electrode and grain boundaries.[7,55] With increasing temperature, the plateaus in ε_r-T plots become frequency-dependent and the maximum temperature of plateaus increases from 75 K (10 kHz) to 105 K (1 MHz). A similar trend is also observed in the $\tan\delta-T$ curves. A like-slope increase of the ε_r-T is accompanied by the appearance of relaxation peaks in $\tan\delta-T$ plots upon heating, owning to the thermal activation-induced hopping of charge carriers and the enhancement of local electric polarization. The relaxation peak of $\tan\delta$ shifts from 82 to 124 K, while the loss values just increase by 0.02 with increasing frequencies, showing a synchronism with the diffusion of ε_r. Figure 4b illustrates the change of $\tan\delta$ with continuous frequencies at different temperatures. Fitting with the Arrhenius equation $f = f_0 \exp(-E_a/k_BT)$ was performed, where f_0 is the frequency factor, E_a is the activation energy and k_B is the Boltzmann constant, yielding E_a = 0.086 eV and $f_0 = 6.1 \times 10^9$ Hz. The low E_a implies that the relaxation comes from the off-center ion hopping,[56] and the large frequency factor of Mn_2MnMoO_6 presents the large size and strong interaction of polar clusters.[57] Unlike the parent Mn_2MnWO_6,[10] the polycrystalline Mn_2MnMoO_6 lacks magnetodielectric and magnetoelectric coupling, as also observed in Mn_2FeMO_6 (M = Nb, Mo, W),[7,9,19] so further investigation on the monodomain single crystal or thin film samples is desired in the future.

CONCLUSIONS

A new exotic perovskite-related polar and magnetic Mn_2MnMoO_6 was prepared at 1673 K and 8 GPa. RT-SPXD measurements of Mn_2MnMoO_6 established a NTO-type ($R3$) polar-corundum structure with all ordered cationic arrangements, giving the estimated large spontaneous polarization of 65.76 $\mu C\cdot cm^{-2}$ and polarization reversal energy barrier around 232 meV. The valence states of Mn and Mo ions were confirmed as $Mn_2^{2+}Mn^{2+}Mo^{6+}O_6$ by crystallographic analysis and X-ray absorption near-edge spectroscopy. Magnetic properties and theoretical calculations indicate two AFM transitions at T_N of 19 and 47 K with the up−down−up−down−up−down ground state in Mn_2MnMoO_6. The geometrically frustrated honeycomb layered motifs render a high magnetic frustration factor of 18.4. The temperature dependence of the dielectric response is magnetic-field (1−5 T) independent and shows no anomalies over the experimental conditions, which suggest the lack of magnetodielectric and magnetoelectric coupling in polycrystalline Mn_2MnMoO_6. These findings further reveal that the physical properties of transition-metal-rich exotic perovskite-based compounds are sensitive to the electron configuration of B cations at certain A-site surroundings; further explorations are necessary for conclusive results, to guide the design of new materials in related categories.

ASSOCIATED CONTENT

Supporting Information

The Supporting Information is available free of charge at https://pubs.acs.org/doi/10.1021/acs.chemmater.1c04357.

Comparison of total candidate magnetic ground-state energies and the magnetic structure for Mn_2MnMoO_6 (Figures S1 and S2); crystallographic parameters of Mn_2MnMoO_6 (Tables S1 and S2) (PDF)

Crystallographic information file for Mn_2MnMoO_6 (CIF)

AUTHOR INFORMATION

Corresponding Authors

Yi-Feng Han − *Key Laboratory of Bioinorganic and Synthetic Chemistry of Ministry of Education, School of Chemistry, Sun Yat-Sen University, Guangzhou 510006, P. R. China*; Email: hanyf26@mail.sysu.edu.cn

Martha Greenblatt − *Department of Chemistry and Chemical Biology, Rutgers, The State University of New Jersey, Piscataway, New Jersey 08854, United States*; orcid.org/0000-0002-1806-2766; Email: greenbla@chem.rutgers.edu

Man-Rong Li − *Key Laboratory of Bioinorganic and Synthetic Chemistry of Ministry of Education, School of Chemistry, Sun Yat-Sen University, Guangzhou 510006, P. R. China*; orcid.org/0000-0001-8424-9134; Email: limanrong@mail.sysu.edu.cn

Authors

Shuang Zhao − *Key Laboratory of Bioinorganic and Synthetic Chemistry of Ministry of Education, School of Chemistry, Sun Yat-Sen University, Guangzhou 510006, P. R. China*

Jin-Jin Yang − *Key Laboratory of Bioinorganic and Synthetic Chemistry of Ministry of Education, School of Chemistry, Sun Yat-Sen University, Guangzhou 510006, P. R. China*

https://doi.org/10.1021/acs.chemmater.1c04357
Chem. Mater. 2022, 34, 1930−1936

Mei-Xia Wu − *Institute of Semiconductors, Guangdong Academy of Sciences, Guangzhou 510650, P. R. China*
Mark Croft − *Department of Physics and Astronomy, Rutgers, the State University of New Jersey, Piscataway, New Jersey 08854, United States*
Peter W. Stephens − *Department of Physics & Astronomy, State University of New York, Stony Brook, New York 11794, United States;* orcid.org/0000-0002-8311-7305
David Walker − *Lamont Doherty Earth Observatory, Columbia University, Palisades, New York 10964, United States*

Complete contact information is available at: https://pubs.acs.org/10.1021/acs.chemmater.1c04357

Notes

The authors declare no competing financial interest.
The supporting crystallographic information file may also be obtained from FIZ Karlsruhe, 76344 Eggenstein-Leopoldshafen, Germany (e-mail: crysdata@fiz-karlsruhe.de), on quoting the deposition number CSD-2118667 (Mn2MnMoO6).

■ ACKNOWLEDGMENTS

This work was financially supported by the National Natural Science Foundation of China (NSFC-21875287, 22090041, 11804404, and 22105228), the China Postdoctoral Science Foundation (2021M693603), the Program for Guangdong Introducing Innovative and Entrepreneurial Teams (2017ZT07C069), and the National Natural Science Foundation of Guangdong Province (Grant No. c18140500000854). The calculations were conducted at the National Supercomputer Center in Guangzhou. The authors thank Dr. Christoph P. Grams and Joachim Hemberger at Universitätzu Köln for their help in magnetic measurements. Use of the NSLS, Brookhaven National Laboratory, was supported by the DOE BES (DE-AC02-98CH10886)

■ ABBREVIATIONS USED

Ps, spontaneous polarization; HPT, high pressure and temperature; RT, room temperature; AP, ambient pressure; NTO, Ni_3TeO_6; OIL, ordered ilmenite; AFM, antiferromagnetic; SPXD, synchrotron powder X-ray diffraction; FM, ferromagnetic; XANES, X-ray absorption near-edge spectroscopy; DFT, density functional theory; PAW, projector augmented wave; GGA, generalized gradient approximation; WL, white line; LF, ligand field; CW, Curie−Weiss; ZFC, zero-field-cooled; FC, field-cooled

■ REFERENCES

(1) Cai, G. H.; Greenblatt, M.; Li, M. R. Polar Magnets in Double Corundum Oxides. *Chem. Mater.* **2017**, *29*, 5447−5457.
(2) Spaldin, N. A.; Fiebig, M. The Renaissance of Magnetoelectric Multiferroics. *Science* **2005**, *309*, 391−392.
(3) Tokura, Y. Multiferroics as Quantum Electromagnets. *Science* **2006**, *312*, 1481−1482.
(4) Spaldin, N. A.; Cheong, S. W.; Ramesh, R. Multiferroics: Past, Present, and Future. *Phys. Today* **2010**, *63*, 38−43.
(5) Han, Y. F.; Wu, M. X.; Gui, C. R.; Zhu, C. H.; Sun, Z. X.; Zhao, M. H.; Savina, A. A.; Abakumov, A. M.; Wang, B.; Huang, F.; He, L. H.; Chen, J.; Huang, Q. Z.; Croft, M.; Ehrlich, S.; Khalid, S.; Deng, Z.; Jin, C. Q.; Grams, C. P.; Hemberger, J.; Wang, X. Y.; Hong, J. W.; Adem, U.; Ye, M.; Dong, S.; Li, M. R. Data-driven Computational Prediction and Experimental Realization of Exotic Perovskite-related Polar Magnets. *npj Quantum Mater.* **2020**, *5*, No. 92.
(6) Oh, Y. S.; Artyukhin, S.; Yang, J. J.; Zapf, V.; Kim, J. W.; Vanderbilt, D.; Cheong, S. W. Non-hysteretic Colossal Magnetoelectricity in A Collinear Antiferromagnet. *Nat. Commun.* **2014**, *5*, No. 3201.
(7) Li, M. R.; Retuerto, M.; Walker, D.; Sarkar, T.; Stephens, P. W.; Mukherjee, S.; Dasgupta, T. S.; Hodges, J. P.; Croft, M.; Grams, C. P.; Hemberger, J.; Sanchez-Benitez, J.; Huq, A.; Saouma, F. O.; Jang, J. I.; Greenblatt, M. Magnetic-Structure-Stabilized Polarization in An Above-Room-Temperature Ferrimagnet. *Angew. Chem., Int. Ed.* **2014**, *53*, 10774−10778.
(8) Li, M. R.; Retuerto, M.; Stephens, P. W.; Croft, M.; Sheptyakov, D.; Pomjakushin, V.; Deng, Z.; Akamatsu, H.; Gopalan, V.; Sanchez-Benitez, J.; Saouma, F. O.; Jang, J. I.; Walker, D.; Greenblatt, M. Low-Temperature Cationic Rearrangement in a Bulk Metal Oxide. *Angew. Chem., Int. Ed.* **2016**, *55*, 9862−9867.
(9) Li, M. R.; Croft, M.; Stephens, P. W.; Ye, M.; Vanderbilt, D.; Retuerto, M.; Deng, Z.; Grams, C. P.; Hemberger, J.; Hadermann, J.; Li, W. M.; Jin, C. Q.; Saouma, F. O.; Jang, J. I.; Akamatsu, H.; Gopalan, V.; Walker, D.; Greenblatt, M. Mn_2FeWO_6: A New Ni_3TeO_6-type Polar and Magnetic Oxide. *Adv. Mater.* **2015**, *27*, 2177−2181.
(10) Li, M. R.; McCabe, E. E.; Stephens, P. W.; Croft, M.; Collins, L.; Kalinin, S. V.; Deng, Z.; Retuerto, M.; Sen Gupta, A.; Padmanabhan, H.; Gopalan, V.; Grams, C. P.; Hemberger, J.; Orlandi, F.; Manuel, P.; Li, W. M.; Jin, C. Q.; Walker, D.; Greenblatt, M. Magnetostriction-polarization Coupling in Multiferroic Mn_2MnWO_6. *Nat. Commun.* **2017**, *8*, No. 2037.
(11) Li, M. R.; Hodges, J. P.; Retuerto, M.; Deng, Z.; Stephens, P. W.; Croft, M. C.; Deng, X. Y.; Kotliar, G.; Sánchez-Benítez, J.; Walker, D.; Greenblatt, M. Mn_2MnReO_6: Synthesis and Magnetic Structure Determination of a New Transition-Metal-Only Double Perovskite Canted Antiferromagnet. *Chem. Mater.* **2016**, *28*, 3148−3158.
(12) Li, M. R.; Retuerto, M.; Deng, Z.; Stephens, P. W.; Croft, M.; Huang, Q. Z.; Wu, H.; Deng, X. Y.; Kotliar, G.; Sanchez-Benitez, J.; Hadermann, J.; Walker, D.; Greenblatt, M. Giant Magnetoresistance in The Half-metallic Double-Perovskite Ferrimagnet Mn_2FeReO_6. *Angew. Chem., Int. Ed.* **2015**, *54*, 12069−12073.
(13) Arévalo-López, A. M.; Stegemann, F.; Attfield, J. P. Competing Antiferromagnetic Orders in The Double Perovskite Mn_2MnReO_6 (Mn_3ReO_6). *Chem. Commun.* **2016**, *52*, 5558−5560.
(14) Arévalo-López, A. M.; McNally, G. M.; Attfield, J. P. Large Magnetization and Frustration Switching of Magnetoresistance in The Double-Perovskite Ferrimagnet Mn_2FeReO_6. *Angew. Chem., Int. Ed.* **2015**, *127*, 12242−12245.
(15) Han, Y. F.; Zeng, Y. J.; Hendrickx, M.; Hadermann, J.; Stephens, P. W.; Zhu, C.; Grams, C. P.; Hemberger, J.; Frank, C.; Li, S. F.; Wu, M. X.; Retuerto, M.; Croft, M.; Walker, D.; Yao, D. X.; Greenblatt, M.; Li, M. R. Universal A-Cation Splitting in $LiNbO_3$-Type Structure Driven by Intrapositional Multivalent Coupling. *J. Am. Chem. Soc.* **2020**, *142*, 7168−7178.
(16) Coelho, A. TOPAS and TOPAS-Academic: An Optimization Program Integrating Computer Algebra and Crystallographic Objects Written in C++. *J. Appl. Crystallogr.* **2018**, *51*, 210−218.
(17) Retuerto, M.; Li, M. R.; Go, Y. B.; Ignatov, A.; Croft, M.; Ramanujachary, K. V.; Hadermann, J.; Hodges, J. P.; Herber, R. H.; Nowik, I.; Greenblatt, M. Magnetic and Structural Studies of The Multifunctional Material $SrFe_{0.75}Mo_{0.25}O_{3-\delta}$. *Inorg. Chem.* **2012**, *51*, 12273−12280.
(18) Whaley, L. W.; Lobanov, M. V.; Sheptyakov, D.; Croft, M.; Ramanujachary, K. V.; Lofland, S.; Stephens, P. W.; Her, J. H.; Tendeloo, G. V.; Rossell, M.; Greenblatt, M. $Sr_3Fe_{5/4}Mo_{3/4}O_{6.9}$, an n = 2 Ruddlesden-Popper Phase: Synthesis and Properties. *Chem. Mater.* **2006**, *18*, 3448−3457.
(19) Li, M. R.; Walker, D.; Retuerto, M.; Sarkar, T.; Hadermann, J.; Stephens, P. W.; Croft, M.; Ignatov, A.; Grams, C. P.; Hemberger, J.; Nowik, I.; Halasyamani, P. S.; Tran, T. T.; Mukherjee, S.; Dasgupta, T. S.; Greenblatt, M. Polar and Magnetic Mn_2FeMO_6 (M = Nb, Ta) with $LiNbO_3$-type Structure High-Pressure Synthesis. *Angew. Chem., Int. Ed.* **2013**, *52*, 8406−8410.

(20) Croft, M.; Sills, D.; Greenblatt, M.; Lee, C.; Cheong, S. W.; Ramanujachary, K. V.; Tran, D. Systematic Mn d-configuration Change in the $La_{1-x}Ca_xMnO_3$ System: A Mn K-edge XAS Study. *Phys. Rev. B* **1997**, *55*, 8726−8732.
(21) Mandal, T. K.; Croft, M.; Hadermann, J.; Van Tendeloo, G.; Stephens, P. W.; Greenblatt, M. La_2MnVO_6 Double Perovskite: a Structural, Magnetic and X-ray Absorption Investigation. *J. Mater. Chem.* **2009**, *19*, 4382−4390.
(22) Veith, G. M.; Greenblatt, M.; Croft, M.; Ramanujachary, K. V.; Hattrick-Simpers, J.; Lofland, S. E.; Nowik, I. Synthesis and Characterization of $Sr_3FeMoO_{6.88}$: An Oxygen-Deficient 2D Analogue of the Double Perovskite Sr_2FeMoO_6. *Chem. Mater.* **2005**, *17*, 2562−2567.
(23) Kresse, G.; Hafner, J. Ab Initio Molecular Dynamics for Liquid Metals. *Phys. Rev. B* **1993**, *47*, 558−561.
(24) Kresse, G.; Hafner, J. Ab Initio Molecular-Dynamics Simulation of the Liquid-Metal-Amorphous-Semiconductor Transition in Germanium. *Phys. Rev. B* **1994**, *49*, 14251−14269.
(25) Kresse, G.; Furthmüller, J. Efficient Iterative Schemes for Ab Initio Total-Energy Calculations Using a Plane-Wave Basis Set. *Phys. Rev. B* **1996**, *54*, 11169−11186.
(26) Kresse, G.; Furthmüller, J. Efficiency of Ab-initio Total Energy Calculations for Metals and Semiconductors Using a Plane-wave Sasis Set. *Comput. Mater. Sci.* **1996**, *6*, 15−50.
(27) Blöchl, P. E. Projector Augmented-wave Method. *Phys. Rev. B* **1994**, *50*, 17953−17979.
(28) Kresse, G.; Joubert, D. From Ultrasoft Pseudopotentials to the Projector Augmented-wave Method. *Phys. Rev. B* **1999**, *59*, 1758−1775.
(29) Perdew, J. P.; Burke, K.; Ernzerhof, M. Generalized Gradient Approximation Made Simple. *Phys. Rev. Lett.* **1996**, *77*, 3865−3868.
(30) Liechtenstein, A. I.; Anisimov, V. I.; Zaanen, J. Density-functional Theory and Strong Interactions: Orbital Ordering in Mott-Hubbard Insulators. *Phys. Rev. B* **1995**, *52*, R5467−R5470.
(31) Liu, C. F.; Zhang, C. K.; Song, H. Q.; Zhang, C. P.; Liu, Y. G.; Nan, X. H.; Cao, G. Z. Mesocrystal MnO Cubes as Anode for Li-ion Capacitors. *Nano Energy* **2016**, *22*, 290−300.
(32) Ochsenbein, S. T.; Chaboussant, G.; Sieber, A.; Güdel, H. U.; Janssen, S.; Furrer, A.; Attfield, J. P. Magnetic Cluster Excitations in the Antiferromagnetic Phase α-$MnMoO_4$. *Phys. Rev. B* **2003**, *68*, No. 092410.
(33) Saravanakumar, B.; Ramachandran, S. P.; Ravi, G.; Ganesh, V.; Sakunthala, A.; Yuvakkumar, R. Transition Mixed-metal Molybdates ($MnMoO_4$) As an Electrode for Energy Storage Applications. *Appl. Phys. A* **2018**, *125*, No. 6.
(34) Clearfield, A.; Moini, A.; Rudolf, P. R. Preparation and Structure of Manganese Molybdates. *Inorg. Chem.* **1985**, *24*, 4606−4609.
(35) Capillas, C.; Tasci, E. S.; Flor, G.; Orobengoa, D.; Perez-Mato, J. M.; Aroyo, M. I. A New Computer Tool at the Bilbao Crystallographic Server to Detect and Characterize Pseudosymmetry. *Z. Krist. Cryst. Mater.* **2011**, *226*, 186−196.
(36) Ye, M.; Vanderbilt, D. Domain Walls and Ferroelectric Reversal in Corundum Derivatives. *Phys. Rev. B* **2017**, *95*, No. 014105.
(37) Ye, M.; Vanderbilt, D. Ferroelectricity in Corundum Derivatives. *Phys. Rev. B* **2016**, *93*, No. 134303.
(38) Zhao, M. H.; Zhu, C.; Sun, Z.; Xia, T.; Han, Y.; Zeng, Y.; Gao, Z.; Gong, Y.; Wang, X.; Hong, J.; Zhang, W.-X.; Wang, Y.; Yao, D. X.; Li, M. R.; Zhu, C.; Sun, Z.; Xia, T.; Han, Y.; Zeng, Y.; Gao, Z.; Gong, Y.; Wang, X.; Hong, J.; Zhang, W.-X.; Wang, Y.; Yao, D. X.; Li, M. R. Methodological Approach to the High-Pressure Synthesis of 2 Nonmagnetic $Li_2B^{4+}B'^{6+}O_6$ Oxides. *Chem. Mater.* **2022**, *34*, 186−196.
(39) Brown, I. D.; Shannon, R. D. Empirical Bond-Strength-Bond-Length Curves for Oxides. *Acta Crystallogr. A* **1973**, *29*, 266−282.
(40) McCarron, E. M.; Calabrese, J. C. The Growth and Single Crystal Structure of a High Pressure Phase of Molybdenum Trioxide: MoO_3-II. *J. Solid State Chem.* **1991**, *91*, 121−125.
(41) Lufaso, M. W.; Woodward, P. M. Prediction of the Crystal Structures of Perovskites Using the Software Program SPuDS. *Acta Crystallogr., Sect. B: Struct. Sci.* **2001**, *57*, 725−738.
(42) Brown, I. D.; Altermatt, D. Bond-valence Parameters Obtained from a Systematic Analysis of the Inorganic Crystal Structure Database. *Acta Crystallogr., Sect. B: Struct. Sci.* **1985**, *41*, 244−247.
(43) Tabuchi, M.; Takahashi, M.; Kanamaru, F. Relation between the Magnetic Transition Temperature and Magnetic Moment for Manganese Nitrides MnN_γ ($0 < \gamma < 1$). *J. Alloys Compd.* **1994**, *210*, 143−148.
(44) Ehrenberg, H.; Schwarz, B.; Weitzel, H. Magnetic Phase Diagrams of α-$MnMoO_4$. *J. Magn. Magn. Mater.* **2006**, *305*, 57−62.
(45) Gaj, J. A. *Semimagnetic Semiconductors. Comprehensive Semiconductor Science and Technology*, InBhattacharya, P.; Fornari, R.; Kamimura, H., Eds.; Elsevier: Amsterdam, 2011; Vol. 2, pp 95−124.
(46) Wong, P. K. J.; Zhang, W.; Bussolotti, F.; Yin, X.; Herng, T. S.; Zhang, L.; Huang, Y. L.; Vinai, G.; Krishnamurthi, S.; Bukhvalov, D. W.; Zheng, Y. J.; Chua, R.; N'Diaye, A. T.; Morton, S. A.; Yang, C. Y.; Ou Yang, K. H.; Torelli, P.; Chen, W.; Goh, K. E. J.; Ding, J.; Lin, M. T.; Brocks, G.; de Jong, M. P.; Castro Neto, A. H.; Wee, A. T. S. Evidence of Spin Frustration in a Vanadium Diselenide Monolayer Magnet. *Adv. Mater.* **2019**, *31*, No. 1901185.
(47) Lee, S.; Lee, W.; Guohua, W.; Ma, J.; Zhou, H.; Lee, M.; Choi, E. S.; Choi, K. Y. Experimental Evidence for a Valence-Bond Glass in the 5*d*1 Double Perovskite Ba_2YWO_6. *Phys. Rev. B* **2021**, *103*, No. 224430.
(48) Nair, H. S.; Chatterji, T.; Strydom, A. M. Antisite Disorder-induced Exchange Bias Effect in Multiferroic Y_2CoMnO_6. *Appl. Phys. Lett.* **2015**, *106*, No. 022407.
(49) Janssen, L.; Andrade, E. C.; Vojta, M. Honeycomb-Lattice Heisenberg-Kitaev Model in A Magnetic Field: Spin Canting, Metamagnetism, and Vortex Crystals. *Phys. Rev. Lett.* **2016**, *117*, No. 277202.
(50) Kim, M. K.; Moon, J. Y.; Oh, S. H.; Oh, D. G.; Choi, Y. J.; Lee, N. Strong Magnetoelectric Coupling in Mixed Ferrimagnetic-Multiferroic Phases of A Double Perovskite. *Sci. Rep.* **2019**, *9*, No. 5456.
(51) Feng, H. L.; Kang, C. J.; Kim, B.; Kim, K.; Croft, M.; Liu, S.; Tyson, T. A.; Stavitski, E.; Zu, R.; Gopalan, V.; Lapidus, S. H.; Frank, C. E.; Shi, Y.; Walker, D.; Greenblatt, M. A Polar Magnetic and Insulating Double Corundum Oxide: Mn_2MnSbO_6 with Ordered Mn(II) and Mn(III) Ions. *Chem. Mater.* **2021**, *33*, 6522−6529.
(52) Solana-Madruga, E.; Alharbi, K. N.; Herz, M.; Manuel, P.; Attfield, J. P. Unconventional Magnetism in The High Pressure 'All Transition Metal' Double Perovskite Mn_2NiReO_6. *Chem. Commun.* **2020**, *56*, 12574−12577.
(53) Ivanov, S. A.; Mathieu, R.; Nordblad, P.; Tellgren, R.; Ritter, C.; Politova, E.; Kaleva, G.; Mosunov, A.; Stefanovich, S.; Weil, M. Spin and Dipole Ordering in Ni_2InSbO_6 and Ni_2ScSbO_6 with Corundum-Related Structure. *Chem. Mater.* **2013**, *25*, 935−945.
(54) Tan, X.; McCabe, E. E.; Orlandi, F.; Manuel, P.; Batuk, M.; Hadermann, J.; Deng, Z.; Jin, C.; Nowik, I.; Herber, R.; Segre, C. U.; Liu, S.; Croft, M.; Kang, C. J.; Lapidus, S.; Frank, C. E.; Padmanabhan, H.; Gopalan, V.; Wu, M.; Li, M. R.; Kotliar, G.; Walker, D.; Greenblatt, M. $MnFe_{0.5}Ru_{0.5}O_3$: an Above-Room-Temperature Antiferromagnetic Semiconductor. *J. Mater. Chem. C* **2019**, *7*, 509−522.
(55) Catalan, G. Magnetocapacitance without magnetoelectric coupling. *Appl. Phys. Lett.* **2006**, *88*, No. 102902.
(56) Bhattarai, M. K.; Pavunny, S. P.; Instan, A. A.; Scott, J. F.; Katiyar, R. S. Effect of off-center ion substitution in morphotropic lead zirconate titanate composition. *J. Appl. Phys.* **2017**, *121*, No. 194102.
(57) Ghoudi, H.; Chkoundali, S.; Raddaoui, Z.; Aydi, A. Structure properties and dielectric relaxation of $Ca_{0.1}Na_{0.9}Ti_{0.1}Nb_{0.9}O_3$ ceramic. *RSC Adv.* **2019**, *9*, 25358−25367.

https://doi.org/10.1021/acs.chemmater.1c04357
Chem. Mater. 2022, 34, 1930−1936